Bioactive Materials 42 (2024) 165–177

Contents lists available at ScienceDirect

Bioactive Materials

journal homepage: www.keaipublishing.com/en/journals/bioactive-materials

A biomimetic upconversion nanoreactors for near-infrared driven H_2 release to inhibit tauopathy in Alzheimer's disease therapy

Qin Zhang [c,d,1], Chuanqi Li [c,d,1], Bohan Yin [a,b,c], Jiaxiang Yan [c], Yutian Gu [c], Yingying Huang [c], Jiareng Chen [c], Xinyue Lao [g], Jianhua Hao [g], Changqing Yi [h], Yi Zhou [i], James Chung Wai Cheung [c], Siu Hong Dexter Wong [a,b,c,**], Mo Yang [c,d,e,f,*]

[a] School of Medicine and Pharmacy, Ocean University of China, Qingdao, 266003, China
[b] Laboratory for Marine Drugs and Bioproducts, Qingdao Marine Science and Technology Center, Qingdao, 266237, China
[c] Department of Biomedical Engineering, The Hong Kong Polytechnic University, 999077, Hong Kong, China
[d] The Hong Kong Polytechnic University Shenzhen Research Institute, Shenzhen, 518000, China
[e] Research Center for Nanoscience and Nanotechnology, The Hong Kong Polytechnic University, Kowloon, 999077, Hong Kong, China
[f] Joint Research Center of Biosensing and Precision Theranostics, The Hong Kong Polytechnic University, Kowloon, 999077, Hong Kong, China
[g] Department of Applied Physics, The Hong Kong Polytechnic University, 999077, Hong Kong, China
[h] Key Laboratory of Sensing Technology and Biomedical Instruments (Guangdong Province), School of Biomedical Engineering, Sun Yat-Sen University, Guangzhou, 510000, China
[i] Zhongshan School of Medicine, Sun Yat-sen University, Guangzhou, 510080, China

ARTICLE INFO

Keywords:
Artificial photosynthesis
Hydrogen therapy
Oxidative stress
Tau hyperphosphorylation
Alzheimer's disease

ABSTRACT

Abnormal hyperphosphorylation of tau protein is a principal pathological hallmark in the onset of neurodegenerative disorders, such as Alzheimer's disease (AD), which can be induced by an excess of reactive oxygen species (ROS). As an antioxidant, hydrogen gas (H_2) has the potential to mitigate AD by scavenging highly harmful ROS such as •OH. However, conventional administration methods of H_2 face significant challenges in controlling H_2 release on demand and fail to achieve effective accumulation at lesion sites. Herein, we report artificial nanoreactors that mimic natural photosynthesis to realize near-infrared (NIR) light-driven photocatalytic H_2 evolution in situ. The nanoreactors are constructed by biocompatible crosslinked vesicles (CVs) encapsulating ascorbic acid and two photosensitizers, chlorophyll *a* (Chl*a*) and indoline dye (Ind). In addition, platinum nanoparticles (Pt NPs) serve as photocatalysts and upconversion nanoparticles (UCNP) act as light-harvesting antennas in the nanoreacting system, and both attach to the surface of CVs. Under NIR irradiation, the nanoreactors release H_2 in situ to scavenge local excess ROS and attenuate tau hyperphosphorylation in the AD mice model. Such NIR-triggered nanoreactors provide a proof-of-concept design for the great potential of hydrogen therapy against AD.

1. Introduction

Alzheimer's disease (AD), a predominant etiology of dementia during aging, is delineated as a persistent and progressive neurodegenerative condition [1,2]. Its impact is primarily manifested within the hippocampus and cortex, two brain regions highly correlated with cognitive and memory performance. The pathological hallmarks of AD are characterized by the accumulation of amyloid-β (Aβ) plaques and insoluble aggregates of abnormally phosphorylated tau (p-tau) proteins, known as intracellular neurofibrillary tangles [3–5]. Despite extensive efforts to develop treatments for targeting these hallmarks, this disease remains incurable due to its complexity and multifaceted nature. So far, therapeutics based on the Aβ aggregation mechanism have been reported to fail in clinical trials [6,7]. Increasing evidence suggests that tau aggregation via hyperphosphorylation is of utmost importance in the pathogenesis of AD [8]. Moreover, AD can also be triggered by a cascade

Peer review under responsibility of KeAi Communications Co., Ltd.
* Corresponding author. Department of Biomedical Engineering, The Hong Kong Polytechnic University, 999077, Hong Kong, China.
** Corresponding author. School of Medicine and Pharmacy, Ocean University of China, Qingdao, 266003, China.
E-mail addresses: dexterwong@ouc.edu.cn (S.H.D. Wong), mo.yang@polyu.edu.hk (M. Yang).
[1] Qin Zhang and Chuanqi Li contributed equally to this work.

https://doi.org/10.1016/j.bioactmat.2024.08.029
Received 29 May 2024; Received in revised form 13 August 2024; Accepted 26 August 2024
Available online 30 August 2024

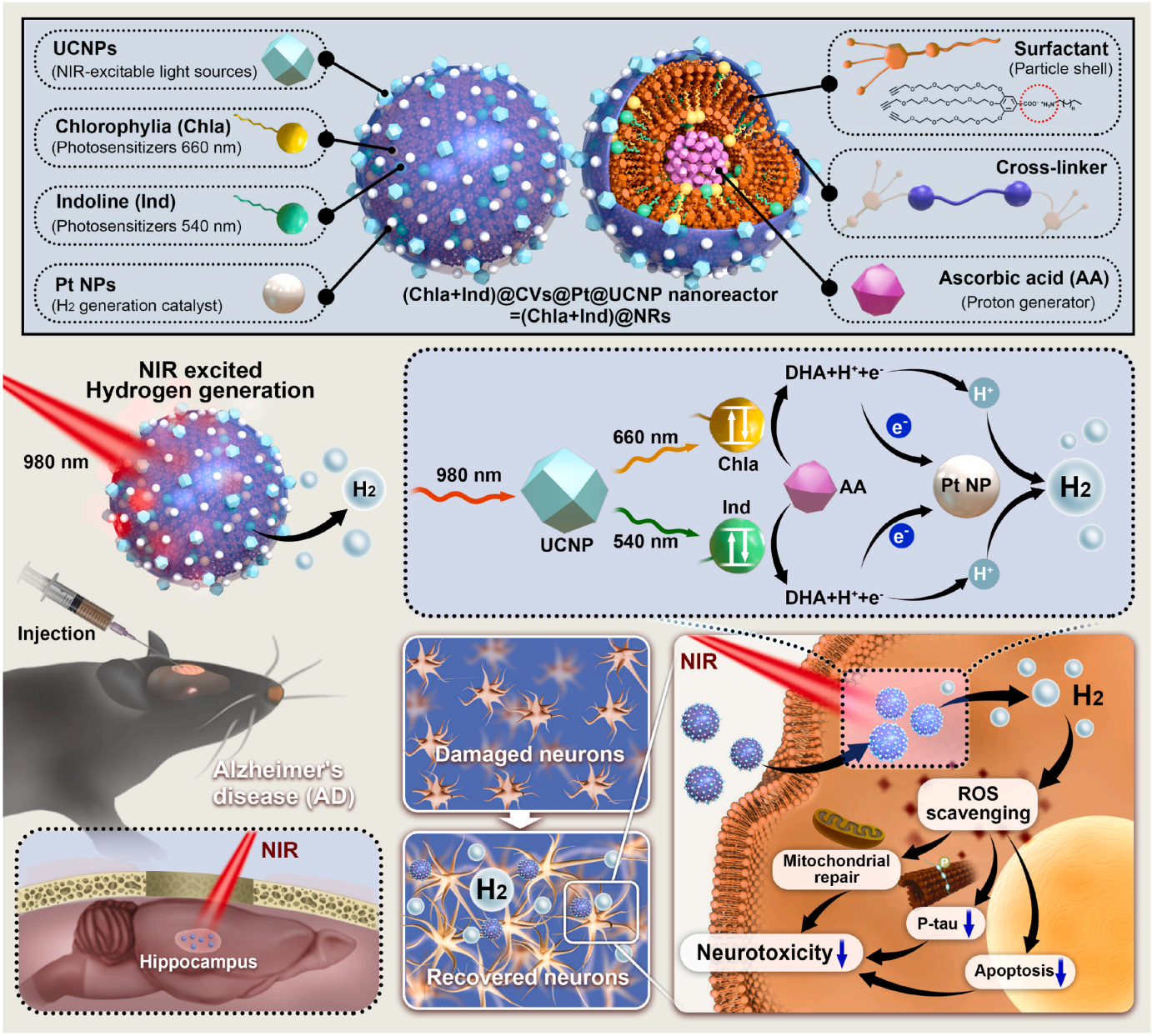

Fig. 1. Schematic diagram illustrating the preparation of (Chl*a* + Ind)@NR and NIR-triggered in situ H_2 release from (Chl*a* + Ind)@NR to scavenge local excess ROS, alleviate mitochondria damage, and reduce tau hyperphosphorylation for AD therapy.

of events involving oxidative stress damage that can lead to tau hyperphosphorylation [9–11]. Thus, antioxidant therapeutic strategies aimed at scavenging excess reactive oxygen species (ROS) to restore brain redox balance have become a prominent approach for treating AD [12].

Recent studies have shown that hydrogen (H_2) gas possesses potent antioxidant properties by selectively scavenging highly cytotoxic ROS, including hydroxyl radical (•OH), peroxynitrite ($ONOO^-$), and hydrogen peroxide (H_2O_2) [13,14]. Hydrogen therapy offers significant advantages over traditional chemotherapy, including minimal side effects and high diffusivity across biological membranes due to its small size and non-polar nature [15]. Currently, H_2 administration can be achieved through three common routes, which include inhalation of H_2, oral intake of H_2-rich water, and injection of H_2-dissolved saline [15,16]. Yet, these methods are ineffective in delivering H_2 to disease foci due to the poor solubility of H_2 (<1.6 ppm) in body fluids [17]. In light of these challenges, developing efficient delivery strategies for the effective accumulation of H_2 at AD sites is of critical importance to augment the therapeutic potential of H_2-based medication for neurodegenerative disorders.

The advancement of nanotechnology has provided versatile strategies to construct a smart-controlled cargo release system. Emerging nanomaterial-based hydrogen therapies have shown promise in treating various inflammatory diseases due to their good physiological stability and bioavailability compared to traditional antioxidant pharmaceuticals like vitamin E and resveratrol, which often suffer from poor absorption, rapid metabolism, and insufficient targeting of brain lesions, limiting their therapeutic efficacy against neurodegenerative diseases [18,19]. However, current hydrogen nanocarriers also face their own set of challenges. For example, nanocarriers such as mesoporous nanostructures or nanogenerators can mediate sustained H_2 accumulation but may lack active targeting ability, leading to an imbalance in intracellular signaling by over-reduction [20]. Hence, developing nanoplatforms for remote control of in situ H_2 generation at disease sites is highly conducive to addressing these limitations. Literature precedents often

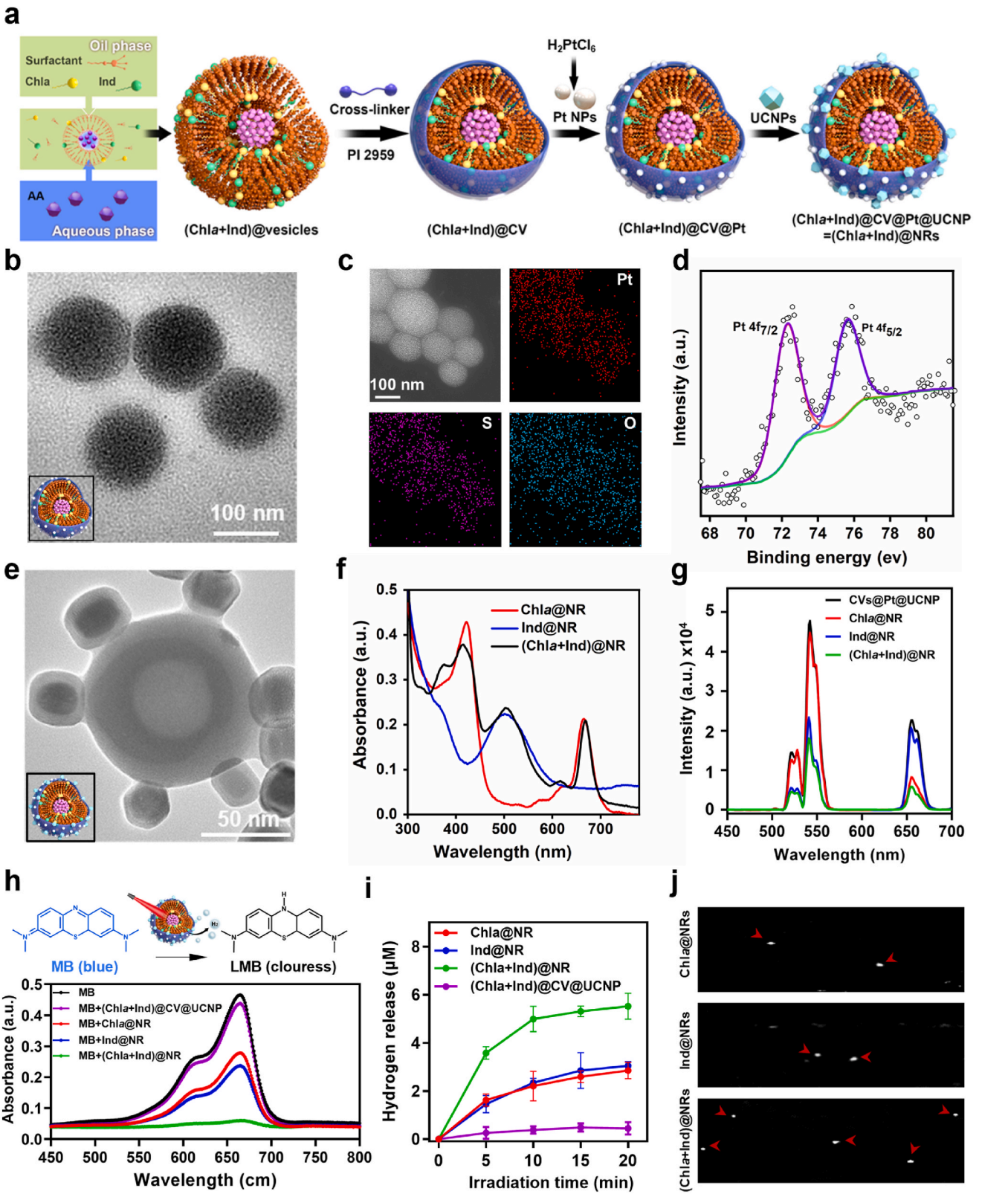

Fig. 2. Preparation and material characterization of (Chl*a* + Ind)@NR. (a) Schematic illustration of the preparation procedure of (Chl*a* + Ind)@NR. (b) TEM images of (Chl*a* + Ind)@CV@Pt. (c) TEM elemental mappings of Pt, O, and S of (Chl*a* + Ind)@CV@Pt. (d) X-ray photoelectron spectra of Pt 4f in (Chl*a* + Ind)@CV@Pt. (e) TEM images of (Chl*a* + Ind)@NR. (f) UV–vis absorbance spectra of Chl*a*@NR, Ind@NR and (Chl*a* + Ind)@NR. (g) Upconversion luminescence spectra of UCNPs, Chl*a*@NR, Ind@NRs and (Chl*a* + Ind)@NR under 980 nm excitation at a power of 0.5 W/cm^2. (h) Top: The reaction mechanism of MB hydrogenation for detecting H_2. MB: methylene blue. LMB: Leucomethylene blue. Bottom: UV–vis absorbance spectra of (Chl*a* + Ind)@CV@UCNP, Chl*a*@NR, Ind@NR and (Chl*a* + Ind)@NR in the MB solution under 980 nm laser irradiation. (i) Quantitative analysis of reductive H_2 release from (Chl*a* + Ind)@CV@UCNP, Chl*a*@NR, Ind@NR and (Chl*a* + Ind)@NR solution using MB as a hydrogen probe under 980 nm laser irradiation for different time duration. (j) Ultrasound images of H_2 bubble generation in Chl*a*@NR, Ind@NR and (Chl*a* + Ind)@NR solution following 980 nm laser (0.5 W/cm^2) irradiation for 10 min.

entail the hydrolysis of metallic hydrides, including calcium [21], magnesium [22], or palladium hydrides [23], as the source of H_2 production in these nanomaterials. Nevertheless, most of these chemicals are usually unstable in aqueous solutions and hence are hard to suppress nonspecific reactions, especially in physiological systems. Recently, artificial photosynthesis-inspired nanoplatforms utilize solar or light energy to photocatalytically decompose water into hydrogen and oxygen, offering an innovative method for in situ photocatalytic H_2 release. Although a few studies have reported on photocatalytic nanoplatform to inhibit Aβ plaques in AD, the effect of photosynthesized H_2 release on the pathological tau phosphorylation remains unexplored (Table S1) [24–31].

Herein, we design a photosynthesis-inspired nanoreactor (NR) that can efficiently exploit near-infrared (NIR) light for photocatalytic H_2 generation to inhibit oxidative stress-mediated tau pathology in AD models (Fig. 1). The architecture of the nanoreacting systems is based on a robustly crosslinked vesicle (CV). This CV provides a confined and stable microenvironment for photocatalytic chemical reactions and serves as a nanocarrier to accommodate the requisite constituents of NIR-responsive photosynthetic systems, involving upconversion nanoparticles (UCNPs), photosensitizers, catalysts, and sacrificial electron donor/proton donor (Fig. 1). To fully harvest the visible light converted from NIR by UCNPs, we innovatively incorporated two photosensitizers, chlorophyll *a* (Chl*a*) and Indoline (Ind) dye, into the nanosystem. Chl*a* is a specific form of chlorophyll, the most common natural photosynthetic pigment that absorbs most optical energy from violet-blue and orange-red light for oxygenic photosynthesis and can be a good component of artificial light-harvesting systems [32]. Similarly, Ind is a well-known synthetic molecule with a high conversion efficiency in biomimetic solar cells and shows strong absorption in the green light region [33]. Hence, Chl*a* can be combined with Ind in our nanoreactors for a nearly full visible light spectrum absorption, significantly enhancing the efficiency of photocatalytic H_2 evolution and distinguishing our nanoreactors from existing nanosystem for artificial photosynthetic H_2 production (Table S2) [24,32,34]. To initiate the H_2 formation, our crosslinked vesicle-bound UCNPs convert NIR irradiation into visible light to excite the photosensitizers (Chl*a* and Ind) that for a dual-effect of electron donation and are subsequently reduced by ascorbic acid (AA), releasing dehydroascorbic acids (DHA) and H^+ as side products [33,34]. Simultaneously, crosslinked vesicle-bound platinum nanoparticles (Pt NPs) rapidly catalyze H_2 evolution via combining the excited electrons and H^+ [35], thereby locally producing a high concentration of therapeutic H_2 gas (Fig. 1 and Fig. S1). In this proof-of-concept work, our results demonstrated that NIR-controlled in situ production of bio-reductive H_2 gas remarkably recovered the ROS homeostasis for in vitro and in vivo AD models. By neutralizing excessive ROS, our nanoreactors triggered (1) the restoration of mitochondrial abnormalities, (2) attenuation of tau hyperphosphorylation through Akt/GSK-3β signaling pathway, and (3) protection of neurons from apoptosis for in vitro AD models under NIR irradiation. Moreover, such a local H_2 generation in the cortex and hippocampus rescued the neuronal density and improved cognitive function by suppressing p-tau pathology in mice of AD models. These mechanistic findings highlight that such a biomimetic strategy of NIR-mediated local delivery of H_2 is potentially a promising approach to counterbalance excessive ROS to resolve tau aggregation and limit the pathogenesis of AD.

2. Results and discussion

2.1. Synthesis and characterization of the photocatalytic nanoreactor for Alzheimer's disease

To prepare our nanoreactors, we first employed the amphiphilic surfactant and thiol-bearing crosslinker to form the crosslinked vesicles as a stable compartment according to our previous method (Figs. S2–3) [36]. Note that this surfactant consists of a hydrophobic tail (hydrocarbon) and a hydrophilic head (oligo-ethyleneglycol with triple alkynyl groups) (Fig. 1). Thus, we loaded the surfactant solution containing Chl*a* and Ind into an aqueous solution containing ascorbic acid to form nanovesicles through self-assembly (Fig. 2a) [37]. To enhance the structural stability, we further added ethylene glycol dithiol as the crosslinker and Irgacure 2959 photoinitiator to enable photocrosslinking to form our crosslinked vesicle that contains photosensitizers, termed [(Chl*a* + Ind)@CV] (Fig. 2a). Based on the standard absorbance curves, the loading efficiencies (LE%) of Chl*a* and Ind were calculated to be 67.7 % and 71.4 %, respectively (Fig. S4). Transmission electron microscope (TEM) visualized the spherical morphology and membrane-like structure of (Chl*a* + Ind)@CV with a physical size of ~110 nm (Figs. S5a–b). Doping Pt NPs via reducing chloroplatinic acid onto the crosslinked vesicle surface, yielding Pt nanodots around the crosslinked vesicle, namely (Chl*a* + Ind)@CV@Pt (Fig. 2b). Energy-dispersive X-ray spectroscopy with mapping analysis indicated the presence of Pt in (Chl*a* + Ind)@CV@Pt nanosystem (Fig. 2c and Fig. S5c). X-ray photoelectron spectroscopy spectra further revealed the deconvoluted peaks of Pt $4f_{7/2}$ and Pt $4f_{5/2}$ doublet at binding energies of 72.1 and 76.2 eV (Fig. 2d) [38].

Afterward, we synthesized core/shell-structured UCNPs with the size of 15 nm that converted NIR into visible photoluminescence of two strong peaks at 542 (green) and 658 nm (red) under 980 nm irradiation (Figs. S6a–c). The upconversion energy migration processes are exhibited in Fig. S6d. Specifically, Yb^{3+} is an ideal sensitizer for 980 nm excitation owing to the $^2F_{7/2} \rightarrow {}^2F_{5/2}$ transition, which matches well with the electronic transition of Er^{3+}. The upconversion emissions of Er^{3+} at 542 and 658 nm are ascribed to the $^2H_{11/2} \rightarrow {}^4I_{15/2}$ and $^4F_{9/2} \rightarrow {}^4I_{15/2}$ transitions, which then transmit and excite Chla and Ind (Chla* and Ind*), leading to electron donation and the generation of electron-hole pairs. Chla* and Ind* then react with ascorbic acid and Pt NPs to generate H_2 and return to their ground states for next round of reaction (Fig. S6d). These two emissions highly overlap with the absorbance peaks of Ind and Chl*a*, respectively (Fig. S7), which potentially enhanced the NIR light harvesting efficiency. We then covalently conjugated the UCNPs to (Chl*a* + Ind)@CV@Pt via strong thiol-metal interactions [39], resulting in the formation of our photocatalytic nanoreactor, hereafter referred to as (Chl*a* + Ind)@NR. TEM imaging confirmed UCNPs stably attaching to (Chl*a* + Ind)@CV@Pt with a size increase of ~28 nm (Fig. 2e). Noticeably, (Chl*a* + Ind)@NR demonstrated similar feature absorption peaks of Chl*a* and Ind (Fig. 2f), while fluorescence intensities at 658 nm (I_{658}) and 542 nm (I_{542}) of (Chl*a* + Ind)@NR decreased by 68.9 % and 61.5 %, compared to that of as-prepared CV@Pt@UCNP without loading photosensitizers (Fig. 2g and Fig. S8). This result indicates that the upconverted photon energy is efficiently transferred to the two photosensitizers. Moreover, the consistent hydrodynamic diameters of (Chl*a* + Ind)@NR in PBS buffer, saline solution, and cell culture medium up to 4 days indicated their colloidal stability and dispersibility (Fig. S9), making them suitable to perform a series of efficient energy transfer in a complex physiological environment.

Next, we investigated the intrinsic catalytic performance of (Chl*a* + Ind)@NR empowered by the surface-bound Pt NPs through H_2O_2 decomposition assay. Accordingly, photosensitizers-containing NR [e.g., Chl*a*@NR, Ind@NR, and (Chl*a* + Ind)@NR] initiated this decomposition process rapidly with an O_2 culminating level exceeding 20 mg/L within 10 min regardless of the photosensitizers content in the NR (Fig. S10). This result encouraged us to explore the overall photocatalytic behavior of our NRs by methylene blue (MB) dye reduction test for indicating H_2 production. NIR-stimulated (Chl*a* + Ind)@CV@UCNP did not trigger a significant effect of H_2-mediated MB reduction (Fig. 2h and Fig. S11), suggesting minimal H_2 release from the nanosystem without Pt NPs. Chl*a*@NR or Ind@NR reduced the MB absorbance at 664 nm to half of the untreated MB group, while (Chl*a* + Ind)@NR nearly reduced all MB to colorless leucomethylene blue (LMB) (Fig. 2h), suggesting that Pt NPs as the catalyst is essential for photocatalytic H_2 production in our

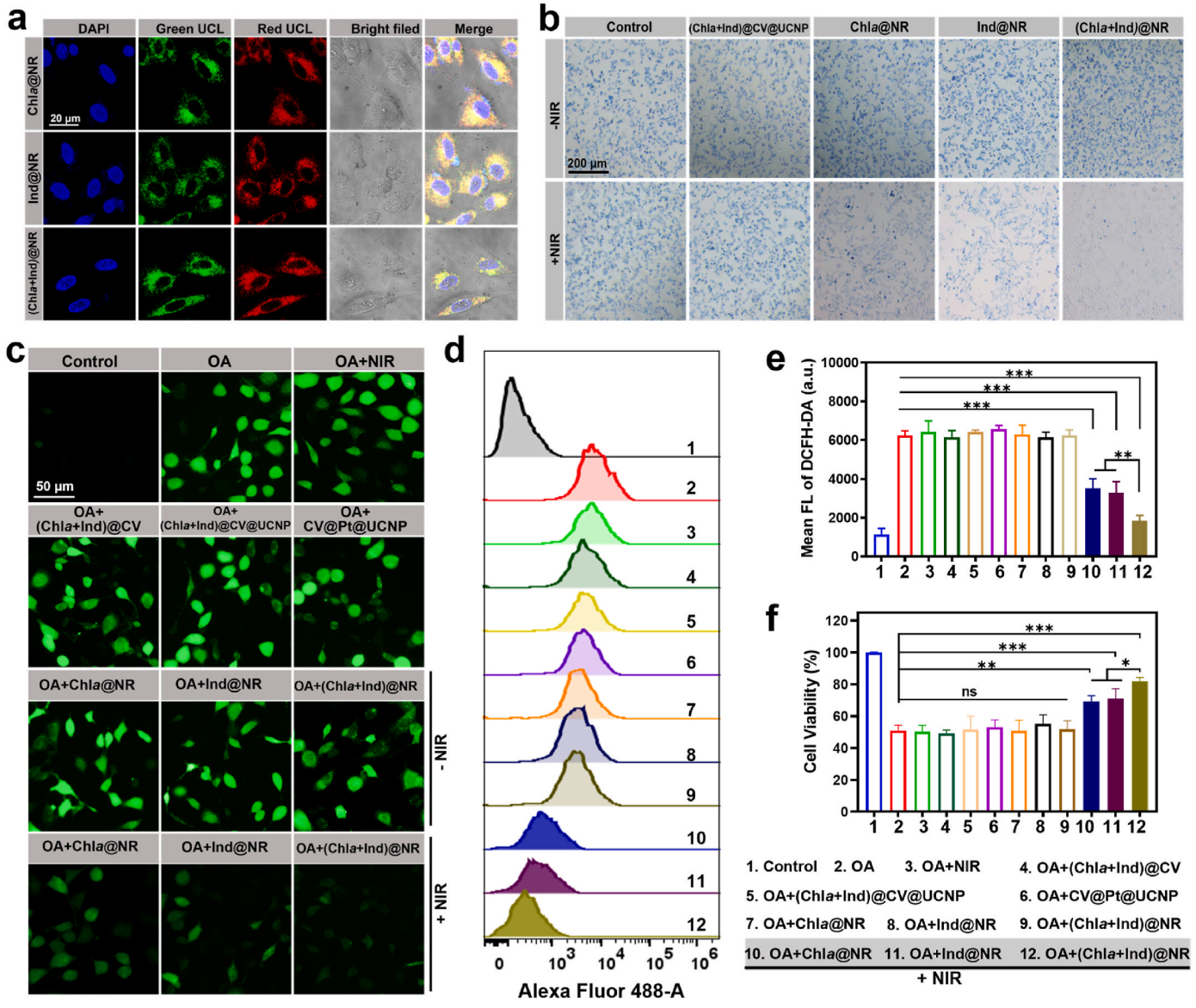

Fig. 3. Investigating the intracellular ROS scavenging capacity of (Chl*a* + Ind)@NR. (a) Confocal microscopic images of PC12 cells after incubation with Chl*a*@NR, Ind@NR and (Chl*a* + Ind)@NR. The images of green upconversion luminescence (UCL) and red UCL were captured under excitation at 980 nm. Scale bar: 20 μm. (b) Qualitative survey of H_2 release from (Chl*a* + Ind)@CV@UCNP, Chl*a*@NR, Ind@NR and (Chl*a* + Ind)@NR in MB-stained PC12 cells. Scale bar: 200 μm. (c) Representative fluorescence images of DCFH-DA indicated intracellular ROS levels. PC12 cells were incubated with OA to induce ROS overproduction, followed by various treatments with/without NIR laser irradiation. (d) Quantitative analysis of intracellular fluorescence intensity of DCFH-DA probe by flow cytometry assay. (e) Statistical results of intracellular fluorescence intensity of DCFH-DA measured by flow cytometry. (f) The relative cell viability of PC12 cells was measured by an MTT assay. The data were presented as mean ± SD (n = 3). Significance: no significance (ns), *p < 0.05, **p < 0.01 and ***p < 0.001.

nanoreactor. Notably, (Chl*a* + Ind)@NR elicited a faster and ~1.8 times more H_2 production than those in Chl*a*@NR and Ind@NR within 10 min (Fig. 2i and Fig. S11). The results reveal that the inclusion of both photosensitizers provides a dual-effect of H_2 generation efficiency by a wider spectrum absorption (red and green upconversion luminescence) compared to those of single photosensitizer-containing nanoreactors at the same concentration. Moreover, we employed an ultrasound imaging system to visualize H_2 bubbles during the reaction. Consistently, the (Chl*a* + Ind)@NR group displayed a greater number of bubbles within the same observable field (Fig. 2j). Thus far, our nanoreactors have demonstrated remarkable capabilities in NIR-triggered photocatalytic H_2 generation. In the following experiments, we continued to include Chl*a*@NR and Ind@NR as the comparison groups to (Chl*a* + Ind)@NR to emphasize the importance of dual-photosensitizer loading in our experimental design.

2.2. Optical control of intracellular ROS scavenging

We first evaluated the cytotoxicity of our nanoplatform on PC12 cells, a rat neuroendocrine cell line model. These cells maintained over 85 % viability upon exposure to nanoreactors at concentrations up to 500 μg/mL (four times our experimental dosage), indicating their high biocompatibility (Fig. S12a). We also assessed the relative viability of PC12 cells after incubation with Chl*a*@NR, Ind@NR, and (Chl*a* + Ind)@NR at a concentration of 100 μg/mL followed by NIR irradiation. The results indicated that the survival rate in all the group remained above 93 % post-irradiation (Fig. S12b), suggesting that this NIR power setting did not cause damage to neural cells. In addition, our nanoreactors are specifically tailored to facilitate H_2 production while minimizing ROS generation under NIR irradiation despite the employment of photosensitizers (Chl*a* and Ind) to absorb upconversion luminescence and donate

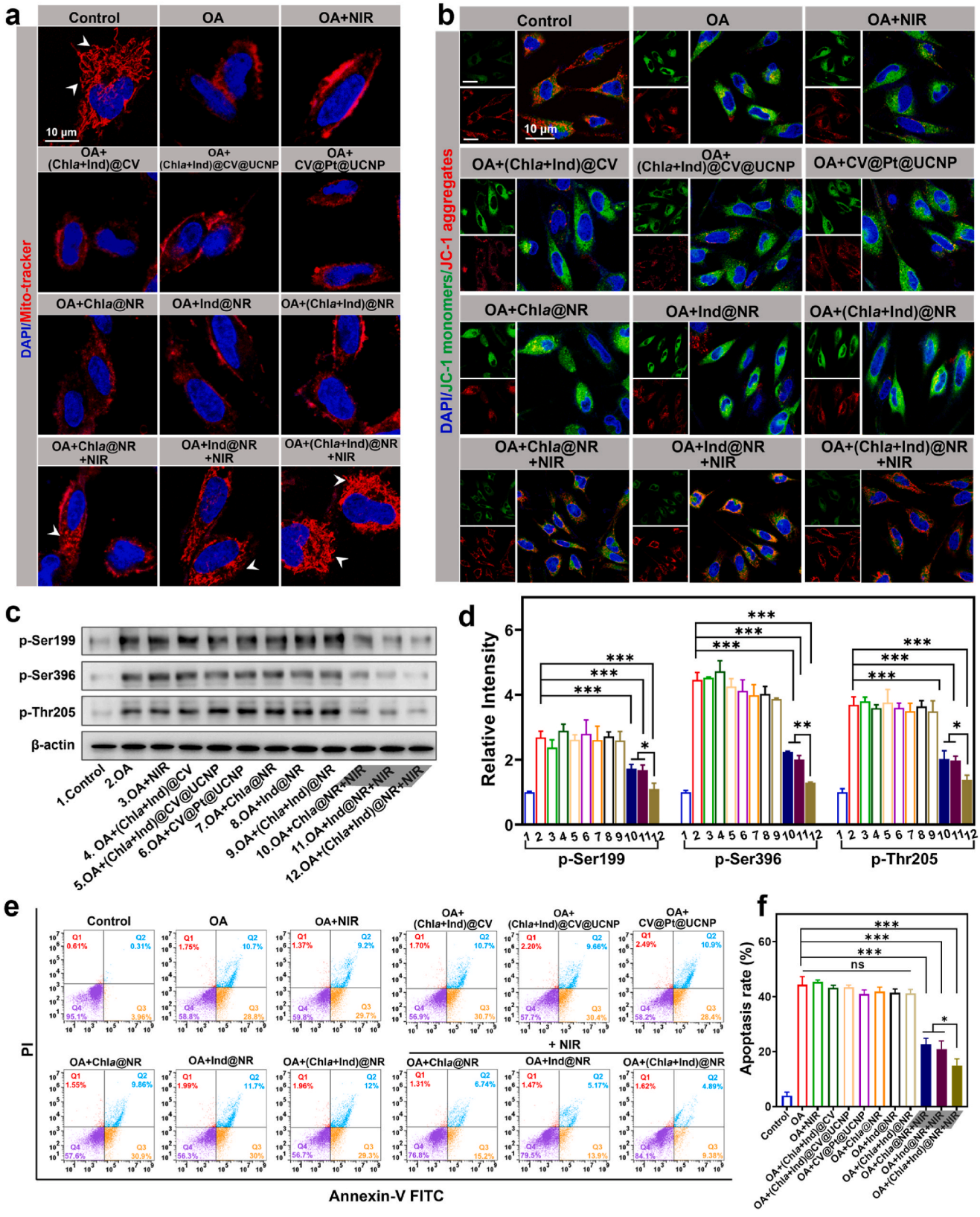

Fig. 4. Investigating the therapeutic effect of (Chl*a* + Ind) NR in vitro. (a) Representative fluorescence images of OA-damaged PC12 cells after various treatments stained with Mito-tracker to display the mitochondrial morphology. The white arrows indicated morphologically normal mitochondria. Scale bar: 10 μm. (b) Representative fluorescence images of OA-damaged PC12 cells after various treatments stained with JC-1 probe to evaluate the mitochondrial membrane potential. Scale bar: 10 μm. (c) Western blot images for p-tau protein at phosphorylated ser199, ser396 epitopes, and thr205 epitopes in PC12 cells after different treatments. (d) Quantification of relative band intensity in western blot images in e) by ImageJ software. (e) The apoptosis results of OA-damaged PC12 cells after incubation with Chl*a*@NR, Ind@NR, and (Chl*a* + Ind)@NR with/without 980 nm laser irradiation were measured by flow cytometry. (f) The quantification results of early and late apoptosis rate in (e). The data were presented as mean ± SD (n = 3). Significance: no significance (ns), *p < 0.05, and ***p < 0.001.

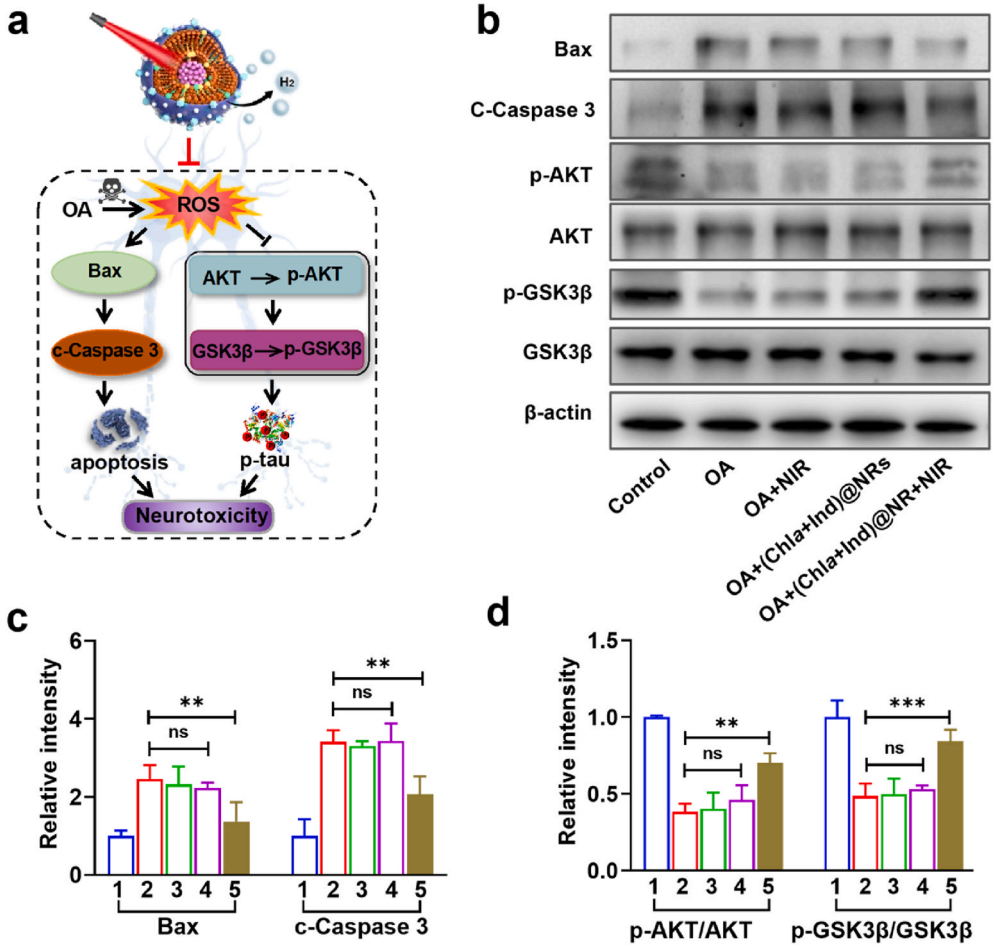

Fig. 5. In vitro therapeutic mechanism of (Chl*a* + Ind)@NR. (a) Proposed model illustrating the mechanism of (Chl*a* + Ind) NR in anti-apoptosis and the amelioration of tau hyperphosphorylation in OA-induced AD cell model. (b) Western blot images for Bax, c-caspase-3, p-Akt (p-Ser473), Akt, p-GSK3*β* (p-Ser9) and GSK3*β* in PC12 cells and OA pre-stimulated PC12 cells, followed by the treatment of different preparations. Quantification results of (c) Bax and caspase-3, (d) p-Akt/Akt and p-GSK3β/GSK3. The levels of Bax and c-caspase-3 were normalized to β-actin. The levels of phosphorylated Akt and phosphorylated GSK3-β were normalized to total Akt and GSK3-β, respectively. Data were presented as mean ± SD (n = 3). Significance: no significance (ns), **p < 0.01 and ***p < 0.001, compare with OA group.

electrons for photocatalytic H_2 production (Fig. S13). These findings indicate that our artificial photosynthetic system is non-toxic to neurons. Subsequently, we assessed the cellular uptake efficiency of our nanoreactors by the cells. Critically, strong red and green upconversion luminescence signals from cytoplasm were captured in all groups [Chl*a*@NR, Ind@NR and (Chl*a* + Ind)@NR] 6 h post uptake, showing good cellular entry of the nanoreactors (Fig. 3a). Notably, the fluorescence intensity of (Chl*a* + Ind)@NR in the cells pretreated with chlorpromazine significantly decreased to only 18.9 % of the untreated group but no obvious fluorescence intensity change was observed for the cells pretreated with nystatin, indicating that these NRs entered cells via a clathrin-mediated endocytic pathway (Fig. S14). To demonstrate the ability of intracellular H_2 generation, we stained PC12 with MB dye, followed by incubating the cells with the nanoreactors. As expected, our in vitro result showed the same trend of MB reduction as those in the solution assays (Fig. 2i) that under NIR control, the blue color of the MB-stained cells drastically faded in Chl*a*@NR, Ind@NR and (Chl*a* + Ind)@NR-treated groups, while no apparent change appeared in (Chl*a* + Ind)@CV@UCNP group (Fig. 3b). Meanwhile, the nanoreactors did not influence the MB staining without NIR irradiation, ascertaining that H_2 was only intracellularly produced by optical control.

To evaluate the ROS eradication capability of (Chl*a* + Ind)@NR, we established an in vitro AD model by treating PC12 cells with okadaic acid (OA) to induce neuronal ROS overproduction and aberrant tau hyperphosphorylation (Fig. S15). We probed the intracellular ROS with a green fluorescent dye, DCFH-DA [40]. Consistently, OA treatment significantly increased ROS levels by 5.2-fold compared to control cells (Fig. 3c–e). We confirmed that NIR stimulation alone and the incompletely constructed NRs with varying contents (e.g., NRs without UCNPs; NRs without Pt NPs as photocatalyst; NRs without photosensitizers) did not mitigate the ROS levels (Fig. 3c–e). In contrast, NIR-mediated suppression of ROS overproduction was successful in the Chl*a*@NR, Ind@NR and (Chl*a* + Ind)@NR groups. In particular, the (Chl*a* + Ind)@NR group outperformed the other two groups in scavenging ROS levels by ~1.9 times and such a ROS level was ~3.2 times lower than those in the untreated control group (Fig. 3c–e), justifying the remote-control functionality of intracellular H_2 production in our NR. As excess ROS can lead to neuronal death [41,42], only 51.6 % of PC12 cells survived in the OA-damaged groups (Fig. 3f). The NIR-stimulated Chl*a*@NR, Ind@NR, and (Chl*a* + Ind)@NR groups effectively promoted the cell survival rates to 70.7 %, 73.1 %, and 82.2 %, respectively (Fig. 3f), while no significant cell viability enhancement in the non-NIR irradiated groups. These findings indicate efficient ROS removal for recovering neuronal damage in the OA model achieved by remote control of H_2 production.

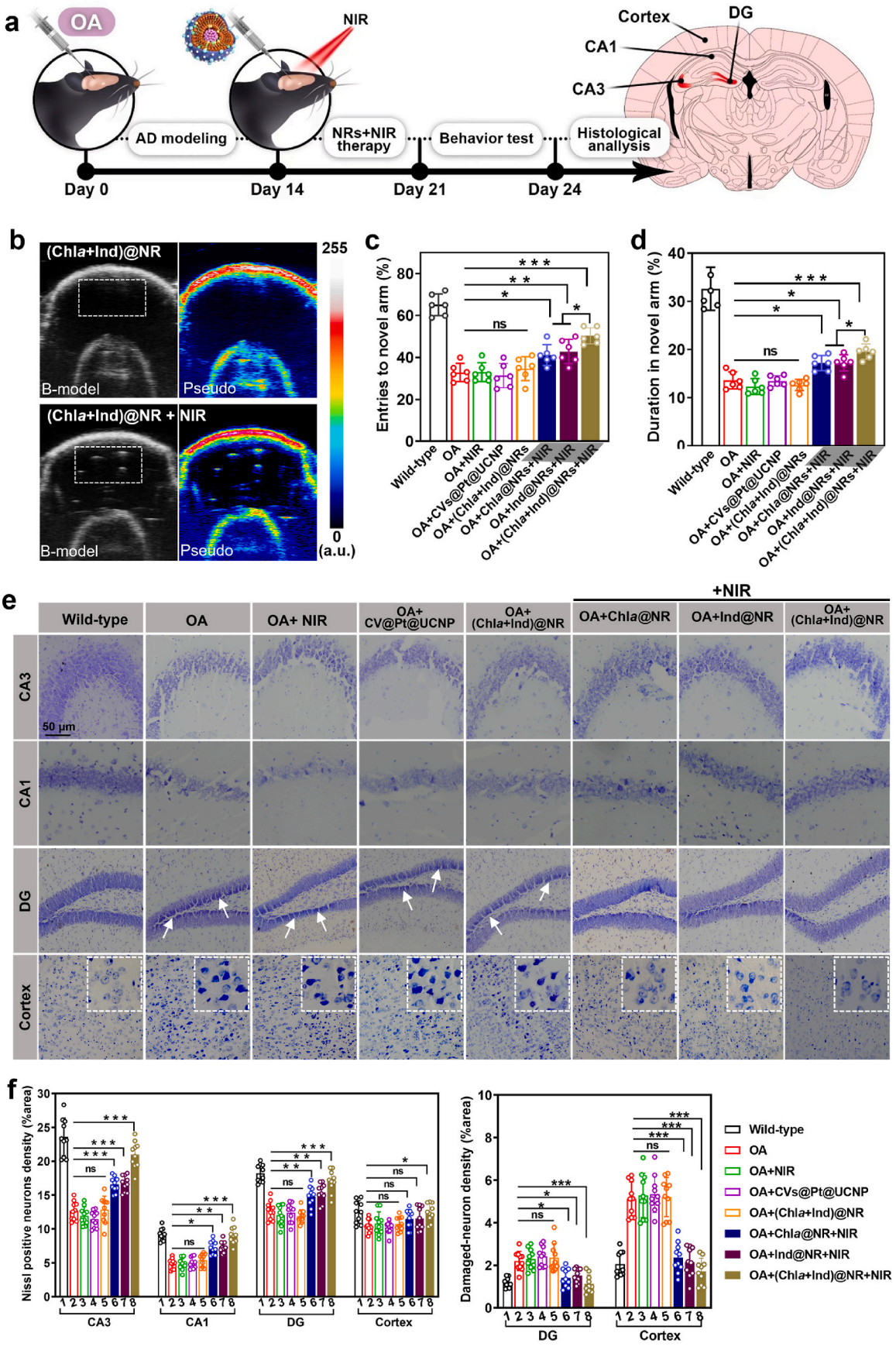

(caption on next page)

Fig. 6. Investigating the therapeutic effect of (Chl*a* + Ind)@NR in AD mice model. (a) Animal experiment flowchart. (b) In vivo ultrasound images obtained in absence or presence of NIR irradiation after the mice were administrated with (Chl*a* + Ind)@NR. Images in the left column were captured using the B-mode of the ultrasound imaging system. Images in the right column represent pseudo-color of the B-mode images. The ROIs (white boxes) showed the ultrasound signal of H_2 bubbles produced in the hippocampus. Quantitative analysis on (c) entry frequency to the novel arm and (d) duration in the novel arm during the test phase in Y maze assay (n = 6). (e) Nissl staining analysis of the density and activity of neurons in the cortex and hippocampus (including CA1, CA3, and DG subregions) of mice brains. The nissl-stained dark cells labeled by the white arrows in DG and white boxes in the cortex represent the typical morphological changes of the damaged neurons. Scale bar: 50 μm. (f) Quantitative results of nissl-positive neurons and nissl-stained dark neurons in the cortex and hippocampus areas. Stained-positive cells in 10 randomly selected fields of view from independent 6 replicates were counted with ImageJ software. Significance: no significance (ns), *$p < 0.05$, **$p < 0.01$ and ***$p < 0.001$.

2.3. NIR-mediated attenuation of tau hyperphosphorylation and apoptosis

Mitochondria play a critical role in biogenesis and respiration, which are fundamentally important for tremendous biochemical processes in virtually all mammalian cells. Mitochondrial dysfunction impacts the pathogenesis of AD. Mitochondrial morphology can reflect its mitochondrial quality and homeostasis. Our results depicted that OA-damaged neuronal cells showed deteriorated and crumpled mitochondrial morphologies, which robustly recovered upon treatment with (Chl*a* + Ind)@NR under NIR irradiation (Fig. 4a). Likewise, membrane potential (ΔΨm) is one of the mitochondrial bioenergetic properties [23,43]. Hence, we probed ΔΨm using JC-1 dye that can form green-fluorescent monomers at low ΔΨm and red-fluorescent aggregates at high ΔΨm [44]. OA-treated cells displayed increased JC-1 monomers and decreased aggregates, with a red/green fluorescence ratio dropping to 31.2 % that of the control, consistent with the result of mitochondrial damage (Fig. 4b and Fig. S16). Incomplete nanoreactors, such as (Chl*a* + Ind)@CV, (Chl*a* + Ind)@CV@UCNP, and CV@Pt@UCNP, did not show significant changes in the red/green fluorescence ratio of JC-1, indicating nearly no improvement in ΔΨm. In contrast, Chl*a*@NR, Ind@NR, and (Chl*a* + Ind)@NR groups with NIR-activation successfully restored the ΔΨm with red/green ratios of 68.8 %, 71.0 % and 80.1 %, respectively (Fig. 4b and Fig. S16). The results indicate effective repair of mitochondrial damage in neural cells by H_2 production. Furthermore, our quantitative analysis of pathogenic p-tau protein indicated that the Chl*a*@NR, Ind@NR, and (Chl*a* + Ind)@NR groups significantly downregulated OA-induced tau hyperphosphorylation at the site of Ser396, Ser199, and Thr205 epitopes under NIR irradiation (Fig. 4c and d). Strikingly, (Chl*a* + Ind)@NR group inhibited p-tau the most compared to those in Chl*a*@NR and Ind@NR groups, thereby offering a promising therapeutic strategy for treating tau pathology. As the reduction of extra ROS and attenuation of tau hyperphosphorylation can prevent neuronal death [45], we further assessed cell apoptosis through flow cytometry of annexin V/propidium iodide-stained cells. As expected, the cell apoptosis rate of OA-damaged cells was 45.8 %. This rate drastically reduced to 14.8 % in the NIR-treated (Chl*a* + Ind)@NR group, of which the apoptosis rate was significantly lower than Chl*a*@NR (24.5 %) and Ind@NR (22.7 %) groups (Fig. 4e and f). These findings underscore the high efficacy of NIR-mediated local H_2 generation in rescuing neurons from apoptosis.

2.4. Downregulation of p-tau and apoptosis signaling for inhibiting neurotoxicity

We further explored the underlying mechanism of (Chl*a* + Ind)@NR to prevent neurons from apoptosis and tau hyperphosphorylation. It is known that oxidative stress can induce apoptosis by activating the pro-apoptotic protein BCL2-associated X (Bax) and the downstream protein caspase 3. Hence, the upregulation of Bax and caspase 3 expressions can trigger the apoptotic cascade signaling (Fig. 5a) [46,47]. Consistently, the protein expression levels of Bax and cleaved caspase 3 (c-Caspase 3) increased in OA-treated cells (Fig. 5b and c) [45], which were remarkably abrogated in the NIR-treated (Chl*a* + Ind)@NR group. In addition to apoptosis, tau pathogenesis in AD involves two main kinases, protein kinase B (Akt) and its downstream kinase glycogen synthase kinase 3β (GSK3β) [42,48]. At regular physiological conditions, phosphorylated Akt (p-Ser473) can trigger GSK3β phosphorylation at residue Ser9 (Fig. 5a) [49,50]. This Akt/GSK3β signaling axis can prevent hyperphosphorylation of tau into p-tau, while ROS is shown to directly oxidize and dephosphorylate Akt, thereby disrupting this signaling [50]. In our results, the OA-treated cells showed suppressed protein levels of p-Akt and p-GSK3β (Fig. 5b and d), consistent with the robust p-tau expression in the in vitro AD model (Fig. 4c). On the other hand, the NIR-stimulated (Chl*a* + Ind)@NR group most effectively reversed this trend under NIR stimulation, thereby indicating the restoration of the Akt/GSK3β signaling pathway to treat tau pathology by our NR. Collectively, we prove that intracellular generation of bio-reductive H_2 markedly downregulates p-tau and apoptosis signaling for inhibiting neurotoxicity guided by NIR light.

2.5. In situ H_2 production for the treatment of murine AD model

We established an in vivo AD model by intracerebral administration of OA in mice to induce oxidative stress and tau hyperphosphorylation within hippocampal and cortical regions, two major areas impacted by AD pathology (Fig. 6a) [51–53]. 14 days post the AD model creation, we injected NRs loaded with IR780-labeled into the hippocampus to track the biodistribution of the NRs via monitoring the fluorescent signal at a regular time interval (Fig. S17a). Notably, the fluorescent intensity at the injection site reached the peak around 2–4 h post-injection, while maintained stably high over 24 h and showed a gradually small decrease 24 h post-injection (Figs. S17b–c). Our ex vivo fluorescence images of the main organs harvested 3 days post-injection showed that the liver and kidney also contained IR780 signals with 4.8 and 8.2 times less than that in the brain (Figs. S17d–e). This result suggests that the bio-trafficking journey of the injected NRs ended with liver and kidney clearance through blood circulation.

To evaluate the therapeutic efficacy in vivo, we stereotactically injected the NRs (Chl*a*@NR, Ind@NR, and (Chl*a* + Ind)@NR) into the unilateral hippocampus of AD mice. 2 h post-injection, we applied NIR laser irradiation on the cranial window to initiate in situ H_2 gas release [24,54]. *In vivo* ultrasound imaging revealed that strong ultrasound signals of H_2 bubbles appeared in the hippocampal regions after administering (Chl*a* + Ind)@NR with NIR irradiation, indicating efficient in situ H_2 gas generation by our nanoreactors (Fig. 6b and Fig. S18). We monitored the local temperature in the brain area covered by NIR laser irradiation. The resulting thermal images denoted that NIR irradiation only slightly generated a thermal effect within 3 °C increment, indicating minimal photothermal harmfulness throughout the NR activation (Fig. S19). Progressive cognitive deficits and memory loss are the primary symptoms of AD. Accordingly, we introduced the Y-maze behavior test to explore the spatial learning and memory ability of AD mice by recording the frequency and duration of novel arm entries [55]. OA-injured AD mice displayed almost half the entry number into the novel arm compared to their wild-type counterparts, indicating a significant impairment in memory function and disrupted exploratory activity (Fig. 6c and d). Neither the photosensitizer-free NR group (CVs@Pt@UCNP) nor the complete NR group [(Chl*a* + Ind)@NR] without NIR irradiation improved the spatial memory performance of AD mice. Remarkably, the NIR excited (Chl*a* + Ind)@NR group enhanced the exploratory behavior of AD mice as evidenced by the

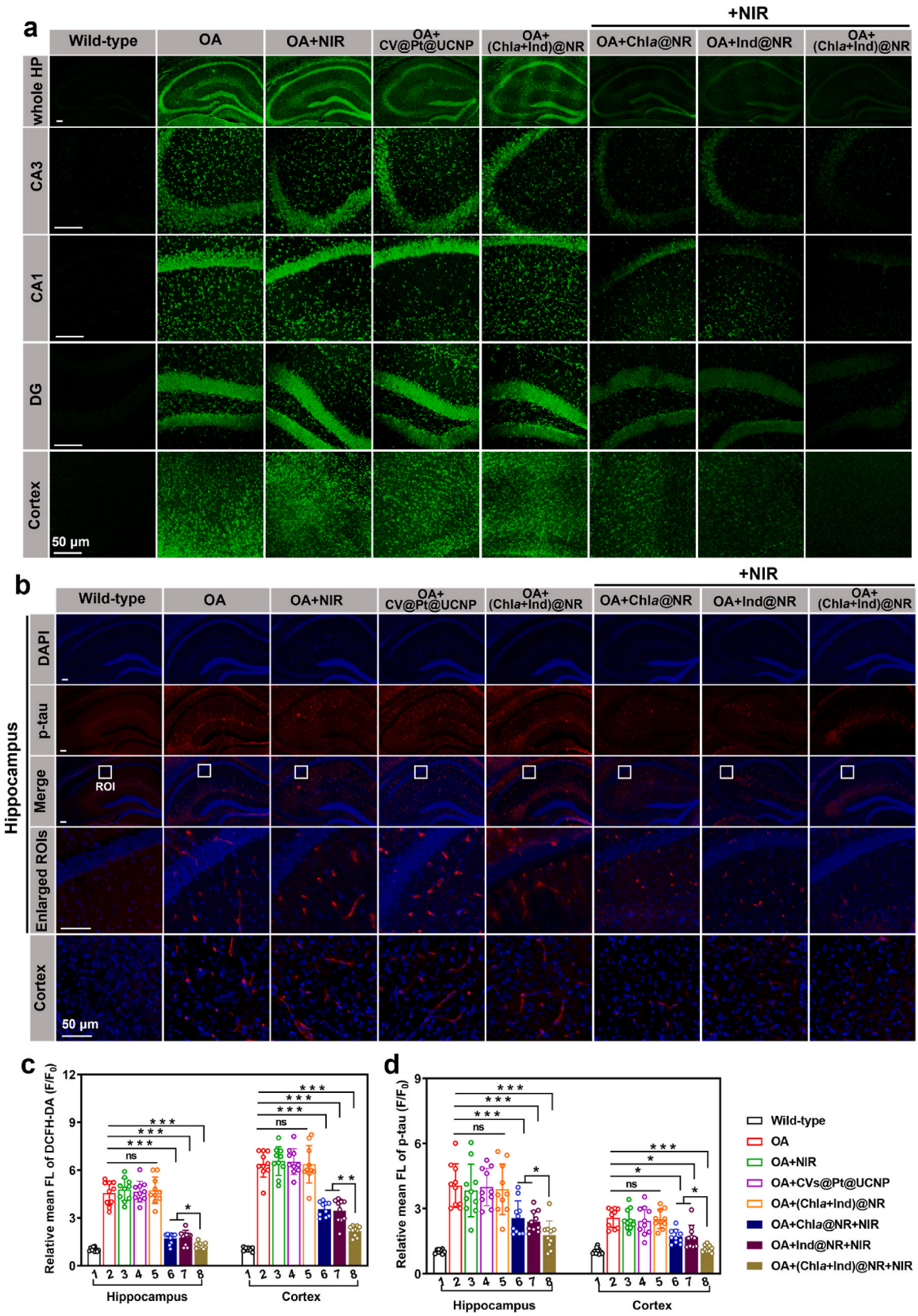

Fig. 7. Ex vivo evaluation of the therapeutic effect of (Chl*a* + Ind)@NR. (a) The fluorescence staining results of ROS indicator DCFH-DA (green) in the whole hippocampus (HP) and enlarged areas in CA1, CA3, DG and cortical regions of wild-type mice and OA induced-AD model mice administered with saline and different NRs (Chl*a*@NRs, Ind@NRs, (Chl*a* + Ind)@NRs) with 980 nm laser irradiation. Scale bar: 50 μm. (b) Immunofluorescence staining with p-tau antibody (red) and DAPI (blue) in the hippocampus and cortex. Scale bar: 50 μm. Quantification of fluorescent intensity of (c) DCFH-DA and (d) p-tau level using ImageJ software. Data were presented as mean ± SD. Significance: no significance (ns), *p < 0.05, **p < 0.01 and ***p < 0.001.

increased duration (from 13.1 % to 19.5 %) and entries (from 31.8 % to 50.3 %) in the novel arm compared to those in the AD mice group (Fig. 6c and d), suggesting restored learning and memory functions. These findings highlight that our biomimetic photosynthetic approach to efficiently generate H_2 in the brain shows great potential in mitigating AD-associated cognitive impairments.

We further performed nissl staining to examine the pathological morphology of neurons in the cortex and hippocampus, specifically in sub-regions of the cornu ammonis 3 (CA3), cornu ammonis 1 (CA1), and dentate gyrus (DG), which encode spatial memory and tau pathogenesis in AD pathology. In OA-induced AD mice without any treatment or treated with NIR alone, the nissl corpuscles showed pale staining, and the stained neurons were atrophied compared to wild-type mice (Fig. 6e). In contrast, the (Chl*a* + Ind)@NR group after NIR irradiation resulted in increased neuronal integrity and more closely arranged cells in CA3 and CA1 areas (Fig. 6e). Quantitative analysis revealed that nissl-positive cell density in (Chl*a* + Ind)@NR-treated AD mice increased to 20.9 % and 9.1 % in CA3 and CA1 respectively, which were greater than those in OA-damaged AD mice (12.7 % and 4.9 % in these two areas) (Fig. 6f). Additionally, the DG and cortical sections in AD mice exhibited more nissl-stained dark cells, representing a typical morphological change of injured neurons [56]. After efficient H_2 production in the (Chl*a* + Ind)@NR group, the nissl-stained dark cells in these sections showed similar staining results as that in the wild-type control (Fig. 6e and f). These findings support the in vivo neuron damage and neurotoxicity alleviation by our nanoreactors.

In addition, we evaluated the ROS levels in the cerebral areas using DCFH-DA probe. Strikingly, ROS levels of the hippocampus and cortex in the AD model were amplified by 4.6 and 6.4 folds compared to the wild-type counterparts (Fig. 7a and c). Administration with CVs@Pt@UCNP and (Chl*a* + Ind)@NR without NIR laser did not affect ROS level (Fig. 7a). An astounding ROS scavenging occurred in groups treated with NRs in the presence of NIR irradiation with the following efficiency order: (Chl*a* + Ind)@NR > Chl*a*@NR ≈ Ind@NR (Fig. 7c). This trend of ROS removal for the in vivo results is consistent with those in the in vitro study (Fig. 3c–e). Moreover, we conducted an immunofluorescence assay to evaluate the expression of p-tau in the brain area. The results demonstrated nearly undetectable p-tau in wild-type mice. However, the AD model showed intense punctate staining of p-tau, with the hippocampal and cortical regions showing 4.1-fold and 2.6-fold higher fluorescent intensity than that of the wild type, respectively (Fig. 7b and d). Obviously, the microinjection of our NRs (Chl*a*@NR, Ind@NR, and (Chl*a* + Ind)@NR) with subsequent NIR laser irradiation significantly mitigated p-tau expression. Specifically, fluorescent signals of p-tau in the hippocampus and cortex of the NIR-triggered (Chl*a* + Ind)@NR group were only ~1.8 and ~1.6 times those in wild-type mice (Fig. 7b and d). Taken together, these histological analyses strongly support that our NRs effectively neutralize ROS overproduction in neuronal cells under NIR irradiation to prevent tau hyperphosphorylation in AD pathology.

Finally, we assessed the in vivo biosafety of the fabricated nanomaterials by performing hematoxylin/eosin (HE) staining on the main organs (heart, liver, spleen, lungs, and kidneys) of mice administrated with Chl*a*@NR, Ind@NR, and (Chl*a* + Ind)@NR (Fig. S20). Compared to the wild-type mice, mice injected with NRs showed no clear histopathological lesions. Furthermore, the hemolysis assay revealed that no hemolysis phenomenon occurred in nanoreactors co-incubation groups, indicating the excellent blood biocompatibility of three types of nanoreactors (Fig. S21). Altogether, our photocatalytic nanoreactors had good biosafety for in vivo applications. Nevertheless, their intracerebral administration method fails to meet the requirements for non-invasive surgery. To enhance translational potential, we aim to optimize the (Chl*a* + Ind)@NR for effective blood-brain barrier penetration and NIR at the second window for better tissue/skull penetration to elicit in situ H_2 production in our future study.

3. Conclusion

In summary, we have developed an NIR-driven artificial nanoreactor that mimics natural photosynthesis to achieve in situ hydrogen gas production for ROS scavenging to treat AD. The artificial NR comprises robustly crosslinked nanovesicle structures with excellent biocompatibility and stability to offer the ideal redox-active compartment for electron transfer in vitro and in vivo. As the stimulation source, NIR light shows low photodamage and deep tissue penetration and is upconverted into visible to excite dual-photosensitizer (Chl*a* + Ind) for artificial photosynthetic hydrogen generation. Mechanistically, the local H_2 delivery efficiently scavenges excessive ROS to reduce the neurotoxicity through suppression of Bax/caspase3 and restoration of Akt/GSK3β signaling to prevent mitochondrial dysfunction/apoptosis and tau hyperphosphorylation in the OA-induced AD model. With this neuroprotection function, the treatment strongly mitigates learning memory deficits and neuronal loss in AD mice. We believe that this proof-of-concept work provides novel insights into the effect of NIR-triggered photocatalytic H_2 on the pathological tau phosphorylation in AD progression, which offers a new approach to hydrogen therapy to inhibit tauopathy for AD treatment.

4. Experimental section

All materials, experimental methods are included in supporting information.

Ethics approval and consent to participate

This study was conducted in accordance with the guidelines approved by the Animal Subjects Ethics Sub-committee of The Hong Kong Polytechnic University (ASESC Case No.: 22-23/307-BME-R-GRF).

CRediT authorship contribution statement

Qin Zhang: Writing – original draft, Investigation, Formal analysis, Data curation, Conceptualization. **Chuanqi Li:** Methodology, Investigation, Data curation, Conceptualization. **Bohan Yin:** Methodology, Investigation. **Jiaxiang Yan:** Formal analysis. **Yutian Gu:** Methodology, Investigation. **Yingying Huang:** Methodology. **Jiareng Chen:** Methodology, Formal analysis, Data curation. **Xinyue Lao:** Investigation. **Jianhua Hao:** Investigation. **Changqing Yi:** Data curation. **Yi Zhou:** Data curation, Resources. **James Chung Wai Cheung:** Data curation, Formal analysis. **Siu Hong Dexter Wong:** Writing – review & editing, Supervision, Conceptualization. **Mo Yang:** Writing – review & editing, Funding acquisition, Conceptualization.

Declaration of competing interest

All authors declare that they have no competing financial interests or personal relationships that could have appeared to influence the work reported in this paper.

Acknowledgements

This work was supported by the Shenzhen Science and Technology Program-Basic Research Scheme (JCYJ20220531090808020), the Research Grants Council (RGC) of Hong Kong Collaborative Research Grant (C5005-23W and C5078-21E), the Research Grants Council (RGC) of Hong Kong General Research Grant (PolyU 15217621 and PolyU 15216622), the Guangdong-Hong Kong Technology Cooperation Funding Scheme (GHP/032/20SZ and SGDX20201103095404018), the Hong Kong Polytechnic University Shenzhen Institute Bai Cheng Bai Yuan Fund (I2022A002), PolyU Internal Fund (1-YWB4, 1-WZ4E, 1-CD8M, 1-WZ4E, 1-CEB1, 1-YWDU, 1-CE2J and 1-W02C). We also would like to acknowledge the funding from the Laboratory for Marine Drugs

and Bioproducts, Qingdao Marine Science and Technology Center (No.: LMDBCXRC202401 and LMDBCXRC202402), Shandong Provincial Overseas Excellent Young Scholar Program (2024HWYQ-042 and 2024HWYQ-043) and Taishan Scholar Youth Expert Program of Shandong Province (tsqn202306102 and tsqn202312105) supporting this work. This work was also supported by the University Research Facility in Life Sciences of the Hong Kong Polytechnic University.

Appendix A. Supplementary data

Supplementary data to this article can be found online at https://doi.org/10.1016/j.bioactmat.2024.08.029.

We developed nanoreactors-(Chl*a* + Ind)@NR that mimic natural photosynthesis to realize near infrared (NIR)-driven photocatalytic H_2 release. By scavenging excessive intracellular reactive oxidant species (ROS), (Chl*a* + Ind)@NR could suppress mitochondrial damage and tau hyperphosphorylation, thereby rescue neurons from apoptosis. With this neuroprotection function, the NR provides novel insights into a new approach to Alzheimer's disease treatment.

References

[1] B. Dubois, H. Hampel, H.H. Feldman, P. Scheltens, P. Aisen, S. Andrieu, H. Bakardjian, H. Benali, L. Bertram, K. Blennow, K. Broich, E. Cavedo, S. Crutch, J. F. Dartigues, C. Duyckaerts, S. Epelbaum, G.B. Frisoni, S. Gauthier, R. Genthon, A. A. Gouw, M.O. Habert, D.M. Holtzman, M. Kivipelto, S. Lista, J.L. Molinuevo, S. E. O'Bryant, G.D. Rabinovici, C. Rowe, S. Salloway, L.S. Schneider, R. Sperling, M. Teichmann, M.C. Carrillo, J. Cummings, C.R. Jack Jr., G. Proceedings of the Meeting of the International Working, A.D. the American Alzheimer's Association on "The Preclinical State of, July, U.S.A. Washington Dc, Preclinical Alzheimer's disease: Definition, natural history, and diagnostic criteria, Alzheimers Dement 12 (3) (2016) 292–323.

[2] M.G. Savelieff, G. Nam, J. Kang, H.J. Lee, M. Lee, M.H. Lim, Development of Multifunctional Molecules as Potential Therapeutic Candidates for Alzheimer's Disease, Parkinson's Disease, and Amyotrophic Lateral Sclerosis in the Last Decade, Chem. Rev. 119 (2) (2019) 1221–1322.

[3] J.J. Palop, L. Mucke, Amyloid-beta-induced neuronal dysfunction in Alzheimer's disease: from synapses toward neural networks, Nat. Neurosci. 13 (7) (2010) 812–818.

[4] J. Wang, Y. Fan, Y. Tan, X. Zhao, Y. Zhang, C. Cheng, M. Yang, Porphyrinic Metal-Organic Framework PCN-224 Nanoparticles for Near-Infrared-Induced Attenuation of Aggregation and Neurotoxicity of Alzheimer's Amyloid-beta Peptide, ACS Appl. Mater. Interfaces 10 (43) (2018) 36615–36621.

[5] J. Wang, Y. Gu, X. Liu, Y. Fan, Y. Zhang, C. Yi, C. Cheng, M. Yang, Near-Infrared Photothermally Enhanced Photo-Oxygenation for Inhibition of Amyloid-beta Aggregation Based on RVG-Conjugated Porphyrinic Metal-Organic Framework and Indocyanine Green Nanoplatform, Int. J. Mol. Sci. 23 (18) (2022).

[6] F. Panza, M. Lozupone, G. Logroscino, B.P. Imbimbo, A critical appraisal of amyloid-βtargeting therapies for Alzheimer disease, Nat. Rev. Neurol. 15 (2) (2019) 73–88.

[7] J. Cummings, Lessons Learned from Alzheimer Disease: Clinical Trials with Negative Outcomes, Cts. Clin. Transl. Sci. 11 (2) (2018) 147–152.

[8] F.M. Ferguson, N.S. Gray, Kinase inhibitors: the road ahead, Nat. Rev. Drug Discov. 17 (5) (2018) 353–376.

[9] Q. Zhang, B. Yin, Y. Huang, Y. Gu, J. Yan, J. Chen, C. Li, Y. Zhang, S.H.D. Wong, M. Yang, A dual "turn-on" biosensor based on AIE effect and FRET for in situ detection of miR-125b biomarker in early Alzheimer's disease, Biosens. Bioelectron. 230 (2023) 115270.

[10] A. Lloret, T. Fuchsberger, E. Giraldo, J. Vina, Molecular mechanisms linking amyloid beta toxicity and Tau hyperphosphorylation in Alzheimer's disease, Free Radic. Biol. Med. 83 (2015) 186–191.

[11] E. Giacobini, G. Gold, Alzheimer disease therapy-moving from amyloid-beta to tau, Nat. Rev. Neurol. 9 (12) (2013) 677–686.

[12] Z.W. Liu, T.Y. Zhou, A.C. Ziegler, P. Dimitrion, L. Zuo, Oxidative Stress in Neurodegenerative Diseases: From Molecular Mechanisms to Clinical Applications, Oxid. Med. Cell. Longev. 2017 (2017).

[13] J. Slezak, B. Kura, T.W. LeBaron, P.K. Singal, J. Buday, M. Barancik, Oxidative Stress and Pathways of Molecular Hydrogen Effects in Medicine, Curr. Pharmaceut. Des. 27 (5) (2021) 610–625.

[14] I. Ohsawa, M. Ishikawa, K. Takahashi, M. Watanabe, K. Nishimaki, K. Yamagata, K. Katsura, Y. Katayama, S. Asoh, S. Ohta, Hydrogen acts as a therapeutic antioxidant by selectively reducing cytotoxic oxygen radicals, Nat. Med. 13 (6) (2007) 688–694.

[15] G. Zhou, E. Goshi, Q. He, Micro/Nanomaterials-Augmented Hydrogen Therapy, Adv. Healthcare Mater. 8 (16) (2019) e1900463.

[16] Y. Wu, M. Yuan, J. Song, X. Chen, H. Yang, Hydrogen Gas from Inflammation Treatment to Cancer Therapy, ACS Nano 13 (8) (2019) 8505–8511.

[17] Q.J. He, Precision gas therapy using intelligent nanomedicine, Biomater. Sci. 5 (11) (2017) 2226–2230.

[18] A. Vaiserman, A. Koliada, A. Zayachkivska, O. Lushchak, Nanodelivery of Natural Antioxidants: An Anti-aging Perspective, Front. Bioeng. Biotechnol. 7 (2019) 447.

[19] R.A. Bohara, N. Tabassum, M.P. Singh, G. Gigli, A. Ragusa, S. Leporatti, Recent Overview of Resveratrol's Beneficial Effects and Its Nano-Delivery Systems, Molecules 27 (16) (2022).

[20] G.X. Zhou, E. Goshi, Q.J. He, Micro/Nanomaterials-Augmented Hydrogen Therapy, Adv. Healthcare Mater. 8 (16) (2019).

[21] F. Gong, J.C. Xu, B. Liu, N.L. Yang, L. Cheng, P. Huang, C.J. Wang, Q. Chen, C.F. Ni, Z. Liu, Nanoscale CaH2 materials for synergistic hydrogen-immune cancer therapy, Chem 8 (1) (2022) 268.

[22] W.L. Wan, Y.J. Lin, P.C. Shih, Y.R. Bow, Q. Cui, Y. Chang, W.T. Chia, H.W. Sung, An In Situ Depot for Continuous Evolution of Gaseous H(2) Mediated by a Magnesium Passivation/Activation Cycle for Treating Osteoarthritis, Angew Chem. Int. Ed. Engl. 57 (31) (2018) 9875–9879.

[23] L. Zhang, P.H. Zhao, C.P. Yue, Z.K. Jin, Q. Liu, X.B. Du, Q.J. He, Sustained release of bioactive hydrogen by Pd hydride nanoparticles overcomes Alzheimer's disease, Biomaterials 197 (2019) 393–404.

[24] K.Z. Ge, Z. Li, A.L. Wang, Z.T. Bai, X. Zhang, X. Zheng, Z. Liu, F.L. Gao, An NIR-Driven Upconversion/C3N4/CoP Photocatalyst for Efficient Hydrogen Production by Inhibiting Electron-Hole Pair Recombination for Alzheimer's Disease Therapy, ACS Nano 17 (3) (2023) 2222–2234.

[25] K. Ge, Y. Mu, M. Liu, Z. Bai, Z. Liu, D. Geng, F. Gao, Gold Nanorods with Spatial Separation of CeO(2) Deposition for Plasmonic-Enhanced Antioxidant Stress and Photothermal Therapy of Alzheimer's Disease, ACS Appl. Mater. Interfaces 14 (3) (2022) 3662–3674.

[26] X. Wang, Q. Han, X. Liu, C. Wang, R. Yang, Multifunctional inhibitors of beta-amyloid aggregation based on MoS(2)/AuNR nanocomposites with high near-infrared absorption, Nanoscale 11 (18) (2019) 9185–9193.

[27] Z. Zhang, J. Wang, Y. Song, Z. Wang, M. Dong, L. Liu, Disassembly of Alzheimer's amyloid fibrils by functional upconversion nanoparticles under near-infrared light irradiation, Colloids Surf. B Biointerfaces 181 (2019) 341–348.

[28] S. Kuk, B.I. Lee, J.S. Lee, C.B. Park, Rattle-Structured Upconversion Nanoparticles for Near-IR-Induced Suppression of Alzheimer's beta-Amyloid Aggregation, Small 13 (11) (2017).

[29] H. Zhang, C. Hao, A. Qu, M. Sun, L. Xu, C. Xu, H. Kuang, Light-Induced Chiral Iron Copper Selenide Nanoparticles Prevent beta-Amyloidopathy In Vivo, Angew Chem. Int. Ed. Engl. 59 (18) (2020) 7131–7138.

[30] Y.V. Stepanov, I. Golovynska, R. Zhang, S. Golovynskyi, L.I. Stepanova, O. Gorbach, T. Dovbynchuk, L.V. Garmanchuk, T.Y. Ohulchanskyy, J. Qu, Near-infrared light reduces beta-amyloid-stimulated microglial toxicity and enhances survival of neurons: mechanisms of light therapy for Alzheimer's disease, Alzheimer's Res. Ther. 14 (1) (2022) 84.

[31] D. Liu, W. Li, X. Jiang, S. Bai, J. Liu, X. Liu, Y. Shi, Z. Kuai, W. Kong, R. Gao, Y. Shan, Using near-infrared enhanced thermozyme and scFv dual-conjugated Au nanorods for detection and targeted photothermal treatment of Alzheimer's disease, Theranostics 9 (8) (2019) 2268–2281.

[32] W.L. Wan, B. Tian, Y.J. Lin, C. Korupalli, M.Y. Lu, Q. Cui, D. Wan, Y. Chang, H. W. Sung, Photosynthesis-inspired H(2) generation using a chlorophyll-loaded liposomal nanoplatform to detect and scavenge excess ROS, Nat. Commun. 11 (1) (2020) 534.

[33] Y. Sun, Y.L. Sun, C. Dall'Agnese, X.F. Wang, G. Chen, O. Kitao, H. Tamiaki, K. Sakai, T. Ikeuchi, S. Sasaki, Dyad Sensitizer of Chlorophyll with Indoline Dye for Panchromatic Photocatalytic Hydrogen Evolution, ACS Appl. Energy Mater. 1 (6) (2018) 2813–2820.

[34] W.L. Wan, Y.J. Lin, H.L. Chen, C.C. Huang, P.C. Shih, Y.R. Bow, W.T. Chia, H. W. Sung, In Situ Nanoreactor for Photosynthesizing H(2) Gas To Mitigate Oxidative Stress in Tissue Inflammation, J. Am. Chem. Soc. 139 (37) (2017) 12923–12926.

[35] J. Wang, Y. Zhong, L. Wang, N. Zhang, R. Cao, K. Bian, L. Alarid, R.E. Haddad, F. Bai, H. Fan, Morphology-Controlled Synthesis and Metalation of Porphyrin Nanoparticles with Enhanced Photocatalytic Performance, Nano Lett. 16 (10) (2016) 6523–6528.

[36] C.Q. Li, S.Y. Zhang, J. Pang, Y. Wu, Z.W. Gu, Facile Fabrication of Robust Organic Counterion-Induced Vesicles: Reversible Thermal Behavior for Optical Temperature Sensor and Synergistic Catalyst upon Removal of Amine, Adv. Funct. Mater. 25 (24) (2015) 3764–3774.

[37] C.Q. Li, J. Zhang, S.Y. Zhang, Y. Zhao, Efficient Light-Harvesting Systems with Tunable Emission through Controlled Precipitation in Confined Nanospace, Angew. Chem., Int. Ed. 58 (6) (2019) 1643–1647.

[38] Y. Chen, J. Tan, Q. Zhang, T. Xin, Y. Yu, Y. Nie, S. Zhang, Artificial Organelles Based on Cross-Linked Zwitterionic Vesicles, Nano Lett. 20 (9) (2020) 6548–6555.

[39] Z.D. Lu, C.B. Gao, Q. Zhang, M.F. Chi, J.Y. Howe, Y.D. Yin, Direct Assembly of Hydrophobic Nanoparticles to Multifunctional Structures, Nano Lett. 11 (8) (2011) 3404–3412.

[40] H.C. Zhang, D.Q. Yu, S.T. Liu, C. Liu, Z.Q. Liu, J.S. Ren, X.G. Qu, NIR-II Hydrogen-Bonded Organic Frameworks (HOFs) Used for Target-Specific Amyloid-b Photooxygenation in an Alzheimer's Disease Model, Angew. Chem., Int. Ed. 61 (2) (2022).

[41] H. Zhou, Y.C. Gong, Y.N. Liu, A.L. Huang, X.F. Zhu, J.W. Liu, G.L. Yuan, L. Zhang, J.A. Wei, J. Liu, Intelligently thermoresponsive flower-like hollow nano-ruthenium system for sustained release of nerve growth factor to inhibit hyperphosphorylation of tau and neuronal damage for the treatment of Alzheimer's disease, Biomaterials 237 (2020).

[42] H. Sun, Y. Zhong, X.D. Zhu, H.W. Liao, J.Y. Lee, Y. Chen, L.J. Ma, J.F. Ren, M. Zhao, M.J. Tu, F.Y. Li, H. Zhang, M. Tian, D.S. Ling, A Tauopathy-Homing and Autophagy-Activating Nanoassembly for Specific Clearance of Pathogenic Tau in Alzheimer's Disease, ACS Nano 15 (3) (2021) 5263–5275.

[43] Y.T. Lin, Q.Q. Shi, L. Zhang, C.P. Yue, Z.J. He, X.X. Li, Q.J. He, Q. Liu, X.B. Du, Hydrogen-rich water ameliorates neuropathological impairments in a mouse model of Alzheimer's disease through reducing neuroinflammation and modulating intestinal microbiota, Neural. Regen. Res. 17 (2) (2022), 409-+.
[44] M. Manczak, P.Z. Mao, M.J. Calkins, A. Cornea, A.P. Reddy, M.P. Murphy, H. H. Szeto, B. Park, P.H. Reddy, Mitochondria-Targeted Antioxidants Protect Against Amyloid-beta Toxicity in Alzheimer's Disease Neurons, J. Alzheimers. Dis. 20 (2010) S609–S631.
[45] L. Chen, Y. Du, K. Zhang, Z.Y. Liang, J.Q. Li, H. Yu, R. Ren, J. Feng, Z.M. Jin, F. Y. Li, J.H. Sun, M. Zhou, Q.G. He, X.L. Sun, H. Zhang, M. Tian, D.S. Ling, Tau-Targeted Multifunctional Nanocomposite for Combinational Therapy of Alzheimer's Disease, ACS Nano 12 (2) (2018) 1321–1338.
[46] L.L. Xu, Y.X. Ding, F.H. Ma, Y. Chen, G.D. Chen, L. Zhu, J.F. Long, R.J. Ma, Y. Liu, J.F. Liu, F. Huang, L.Q. Shi, Engineering a pathological tau-targeted nanochaperone for selective and synergetic inhibition of tau pathology in Alzheimer's Disease, Nano Today 43 (2022).
[47] R.C. Taylor, S.P. Cullen, S.J. Martin, Apoptosis: controlled demolition at the cellular level, Nat. Rev. Mol. Cell Biol. 9 (3) (2008) 231–241.
[48] S.Y. Aghdam, S.W. Barger, Glycogen synthase kinase-3 in neurodegeneration and neuroprotection: Lessons from lithium, Curr. Alzheimer Res. 4 (1) (2007) 21–31.
[49] Y. Kitagishi, A. Nakanishi, Y. Ogura, S. Matsuda, Dietary regulation of PI3K/AKT/GSK-3beta pathway in Alzheimer's disease, Alzheimer's Res. Ther. 6 (3) (2014) 35.
[50] G.C. Han, K.W. Bai, X.Y. Yang, C.H. Sun, Y. Ji, J.P. Zhou, H.Q. Zhang, Y. Ding, "Drug-Carrier" Synergy Therapy for Amyloid-beta Clearance and Inhibition of Tau Phosphorylation via Biomimetic Lipid Nanocomposite Assembly, Adv. Sci. 9 (14) (2022).
[51] H.M. Zhang, X.J. Wang, P. Xu, X.F. Ji, T.Y. Chi, P. Liu, L.B. Zou, Tolfenamic acid inhibits GSK-3 beta and PP2A mediated tau hyperphosphorylation in Alzheimer's disease models, J. Physiol. Sci. 70 (1) (2020).
[52] N. Rajasekar, S. Dwivedi, S.K. Tota, P.K. Kamat, K. Hanif, C. Nath, R. Shukla, Neuroprotective effect of curcumin on okadaic acid induced memory impairment in mice, Eur. J. Pharmacol. 715 (1–3) (2013) 381–394.
[53] N. Broetto, F. Hansen, G. Brolese, C. Batassini, F. Lirio, F. Galland, J.P.A. dos Santos, M.F. Dutra, C.A. Goncalves, Intracerebroventricular administration of okadaic acid induces hippocampal glucose uptake dysfunction and tau phosphorylation, Brain Res. Bull. 124 (2016) 136–143.
[54] C.J. Du, W. Feng, X.Y. Dai, J.H. Wang, D.Y. Geng, X.D. Li, Y. Chen, J. Zhang, Cu2+-Chelatable and ROS-Scavenging MXenzyme as NIR-II-Triggered Blood-Brain Barrier-Crossing Nanocatalyst against Alzheimer's Disease, Small 18 (39) (2022).
[55] N. Hamidi, A. Nozad, H.S. Milan, M. Amani, Okadaic acid attenuates short-term and long-term synaptic plasticity of hippocampal dentate gyrus neurons in rats, Neurobiol. Learn. Mem. 158 (2019) 24–31.
[56] H. Ooigawa, H. Nawashiro, S. Fukui, N. Otani, A. Osumi, T. Toyooka, K. Shima, The fate of Nissl-stained dark neurons following traumatic brain injury in rats: difference between neocortex and hippocampus regarding survival rate, Acta Neuropathol. 112 (4) (2006) 471–481.